Pseudo-ductile compressive behaviour of unidirectional thin-ply carbon/glass fibre-epoxy hybrid composites

Suwarta, Putu; Wisnom, Michael R.; Fotouhi, Mohamad; Wu, Xun; Czél, Gergely

DOI
10.1016/j.compositesa.2025.108877

Publication date
2025

Document Version
Final published version

Published in
Composites Part A: Applied Science and Manufacturing

Composites: Part A 195 (2025) 108877

Contents lists available at ScienceDirect

Composites Part A

journal homepage: www.elsevier.com/locate/compositesa

Pseudo-ductile compressive behaviour of unidirectional thin-ply carbon /glass fibre-epoxy hybrid composites

Putu Suwarta [a,b], Michael R. Wisnom [a], Mohamad Fotouhi [c], Xun Wu [a,d], Gergely Czél [e,f,*]

[a] Bristol Composites Institute, University of Bristol, Queen's Building, University Walk, Bristol BS8 1TR, United Kingdom
[b] Department of Mechanical Engineering, Institut Teknologi Sepuluh Nopember, Surabaya 60111, Indonesia
[c] Department of Materials, Mechanics, Management and Design (3MD), Delft University of Technology, Mekelweg 5, 2628 CD Delft, Netherlands
[d] Faculty of Engineering and Physical Sciences, University of Southampton, University Rd, Southampton SO17 1BJ, United Kingdom
[e] Department of Polymer Engineering, Faculty of Mechanical Engineering, Budapest University of Technology and Economics, Műegyetem rkp. 3, H-1111 Budapest, Hungary
[f] MTA-BME Lendület Sustainable Polymers Research Group, Műegyetem rkp. 3, H-1111 Budapest, Hungary

ARTICLE INFO

Keywords:
Hybrid Composites
Thin-Ply
Unidirectional
Compression
Fragmentation

ABSTRACT

Favourable pseudo-ductile behaviour under compressive loading with a knee-point was achieved for unidirectional (UD) interlayer hybrids made of thin-ply high modulus carbon/epoxy (CF/EP) layers sandwiched between standard thickness glass/epoxy (GF/EP). The UD thin-ply hybrids were tested under two loading scenarios: 1. Direct compressive loading, 2. Four-point bending loading. In both cases, the damage mechanisms responsible for the pseudo-ductile behaviour are fragmentation of the carbon layer and localised delamination, which later propagates unstably. The final failure of the UD thin-ply hybrid composites examined in four-point bending loading occurs at a higher strain than that under direct compressive loading. This is due to the strain gradient in bending, which results in a lower energy release rate than in direct compression. An increasing carbon layer thickness reduces the final delamination failure strain of the UD thin-ply hybrid composites in compression, but the knee-point strain is not affected.

1. Introduction

Composites showing pseudo-ductility under tensile loading have been successfully developed as a new generation of fibre-reinforced polymers (FRP) to alleviate the catastrophic failure of carbon fibre composites [1]. One effective approach is by hybridising fibres with different stiffness and strain at failure, e.g. [2]. Contrary to conventional carbon fibre composites that fail in a sudden and brittle manner, these pseudo-ductile composites are designed to behave more like metals, with a linear elastic and pseudo-plastic deformation regime. One of the basic strategies to achieve pseudo-ductility is to incorporate the damage suppression ability of thin composite layers [3–8] into unidirectional (UD) composite laminates. The high-stiffness and low-strain thin carbon/epoxy (CF/EP) layers sandwiched between high-strain glass/epoxy (GF/EP) layers display favourable gradual damage by fragmentation, suppressing unstable delamination after the first fracturing of the low strain layers due to the low energy released [2,9]. Previous research on UD thin-ply hybrid composites suggests that the pseudo-ductile properties, such as initial modulus, pseudo-yield point, and pseudo-ductile strain, depend on the material properties and suitable values of relative thicknesses (i.e., the thickness ratio of the high stiffness and low-strain material (LSM) and high-strain material (HSM)) and absolute thicknesses of the high stiffness and low-strain material, as reported in [10,11].

Previous investigations to achieve pseudo-ductility in UD thin-ply hybrid composites have primarily focused on tension, but compressive strength is also critical for composite structures. Failure in compressive loading is typically by micro-buckling, due to shear instability of the fibres in the surrounding matrix and is easily affected by defects such as ply waviness and initial ply or fibre misalignment [12–16]. For unidirectional (UD) standard thickness, carbon composite laminates loaded in compression, sudden and catastrophic brittle failure usually occurs [17,18]. The compression strength of composite laminates can be increased by using thin-ply prepregs, due to a more uniform microstructure, better fibre alignment, and smaller resin-rich regions, postponing the micro-buckling, as reported in [7,19,20]. Although the

* Corresponding author.
E-mail address: czel.gergely@gpk.bme.hu (G. Czél).

https://doi.org/10.1016/j.compositesa.2025.108877
Received 26 January 2025; Received in revised form 17 March 2025; Accepted 18 March 2025
Available online 21 March 2025

compression strength of the thin-ply composites increases compared to the standard-thickness composites, their final failure is still brittle and catastrophic.

The studies mentioned above were concerned with standard modulus carbon fibre [20], intermediate modulus carbon fibre [19] and high modulus carbon fibre [7]. For applications where high structural stiffness and low density are needed, high modulus carbon fibre composite is an attractive choice. The compression testing of high-modulus M55J carbon fibre composite laminates with a thickness of 2.22 mm via a bending test by Montagnier et al. [21] showed that the compression failure of the high-modulus carbon fibre composite occurs catastrophically at −0.311 % strain without any warning.

Progressive fracture of hybrids of UD high-modulus M55J carbon/epoxy (CF/EP) layer with a nominal thickness of 0.064 mm under flexural loading with the CF/EP layer located at the compression side was observed by Czél et al. [22]. The thin high-modulus CF/EP layer was sandwiched between several high-strain GF/EP plies, thus avoiding sudden failure due to the load transfer ability between the fractured carbon and intact glass layers. A noticeable slope change at around −0.50 % strain was reported due to fragmentation of the high-modulus CF/EP layer. The fractured CF/EP layer in that work [22] did not show any sign of micro-buckling because the fibres in the thin CF/EP layer failed first. Based on the previous work [22], UD thin-ply hybrid composites under compressive loading can potentially show pseudo-ductility when high-strain glass plies surround the high-modulus thin carbon plies.

Two methods can be used to assess the compression properties of UD thin-ply hybrid composites: (1) direct uniaxial compression and (2) flexural tests (indirect compression). In the first, the load is introduced directly into the material via shear and end loading using a direct uniaxial compression method, e.g.[23]. This test method avoids the strain gradients, which could increase the compressive strain to failure of the UD thin-ply hybrid composites [24]. The drawback of using a direct uniaxial compression loading test is premature failure at the grips, and the end-tabbing and precision machining of the specimen so it has parallel and straight edges [23]. An advantage of using the flexural test [22] is the simple test method, and cheap specimen preparation without end-tabbing and precision machining (e.g., grinding). In this case, the investigated composite layer is put on the compression side as part of a thicker UD composite material coupon. Nevertheless, flexure is a complex loading case that involves a strain gradient through the thickness of the specimen which may raise concerns about the validity of the failure strain measured.

This is the first paper to explain the detailed failure mechanisms responsible for the pseudo-ductile behaviour of UD thin-ply hybrid composites loaded in compression. It also explores the effects of using different thickness high-modulus CF/EP layers on the compressive failure behaviour of UD thin-ply hybrid composites. Some initial results showing the pseudo-ductility of UD thin-ply hybrid composites under direct uniaxial compressive loading were reported by Suwarta et al. [25] but the detailed damage mechanisms were not reported. No CF/EP layer fragmentation was reported in previous work examining the compressive behaviour of carbon fibre-reinforced composites [12–20]. Although Czél et al. [22] observed fragmentation of the M55J CF/EP layer in the UD thin-ply hybrid composites with two M55J CF/EP plies under flexural loading, the effect of different thicknesses of M55J CF/EP layers was not investigated.

The present study is a comprehensive and detailed investigation of combining the benefits of hybrid and thin-ply approaches to produce pseudo-ductility for UD thin-ply hybrid composites under compressive loading. It is also unique in comparing behaviour in two different loading modes: (1) direct uniaxial compression and (2) flexural tests.

2. Experimental methods

2.1. Materials

Standard thickness S-glass/epoxy and E-glass/epoxy supplied by Hexcel and thin M55J carbon/epoxy supplied by North Thin-ply Technology were used in this study. The epoxy resin systems in the prepregs were the aerospace grade 913 (Hexcel) and ThinPreg 120 EPHTg-402 (North TPT). The carbon fibre was a Torayca M55J, classified as high-modulus (HM) grade, and produced in 6000 filament tows [26]. Properties of the applied fibre and prepreg systems can be found in Table 1 and Table 2, respectively. The fibre properties in Table 1 are based on the manufacturer's data and were determined from impregnated strands except for the S-glass, where single-fibre tests were performed.

2.2. Specimen design

2.2.1. Specimen design for direct uniaxial compression testing

Alternating lay-up sequences of standard thickness S-glass/epoxy (S-GF/EP) and thin M55J carbon/epoxy (CF/EP) as shown in Table 3 were chosen to examine the direct uniaxial compression response of UD thin-ply hybrid composites. S-GF/EP layers on either side of the CF/EP layers provide support. The alternating lay-up sequence also allows shear load transfer between the CF/EP layers and the GF/EP layers after the fracture of the CF/EP layers. The geometry of the hybrid specimens examined under uniaxial compressive loading has a nominal width (w) of 10 mm to fit the Imperial College loading rig developed by Häberle et al. [23], and the schematic of the specimen geometry is shown in Fig. 1. A chamfer was introduced into the end tabs to introduce less stress concentration at the tab-tip region of the specimen and thus prevent premature failure near the gripping area, as dictated in the study by Xie et al. [30]. A gauge length of 12 mm was chosen to yield a slenderness ratio below 20 (12.6, 10.9, 9.6 for $[SG_1/(M55_1/SG_1)_{17}]$, $[SG_1/(M55_2/SG_1)_{17}]$, and $[SG_1/(M55_3/SG_1)_{17}]$, respectively), which is estimated to be sufficient to prevent buckling for the hybrid composite laminate [23].

The hybrid specimen configurations, nominal dimensions of the hybrid specimens and the number of carbon plies for direct uniaxial compression testing are shown in Table 3.

2.2.2. Specimen design for indirect compression (four-point bending) testing

In addition to the direct compression test results, a four-point bending (4 PB) setup was chosen to examine if the strain gradient affects the failure mechanisms and strains. The investigated test specimens were asymmetric, with a single block of carbon plies located above the neutral axis (N.A.) close to the specimen's compression side surface, as shown in Fig. 2.

In this work, the number of investigated carbon plies within the single CF/EP layer was 1, 2 and 3. High-strain S-glass/epoxy (S-GF/EP) plies were added on both sides of the CF/EP layer and to the tension side near the surface where the highest tensile strain is expected. Standard thickness E-glass/epoxy (E-GF/EP) plies were used elsewhere to reduce material cost. The higher compressive strain of S-GF/EP compared to the compressive strain to failure of CF/EP suggests that when the carbon layer fractures, the GF/EP will still be intact and support the CF/EP layer.

Three different asymmetric hybrids were examined in four-point bending loading and are shown in Table 4, along with the lay-up sequences, nominal dimensions of the hybrid specimens, and the loading setup. The notations h, w, and L in Table 4 are the measured total thickness, width, and total length of the hybrid specimens, respectively. The specimens were designed to be relatively thick to ensure significant surface strains on the compression side at relatively small deflections while minimising the corresponding geometric non-linearity of the load–deflection response.

Table 1
Fibre properties of the applied UD prepregs based on the manufacturer's data [22].

Fibre type	Manufacturer	Tensile modulus	Tensile strain to failure	Tensile strength	Density	CTE α_{11}
		[GPa]	[%]	[GPa]	[g/cm^3]	[1/K]
Torayaca M55J	Toray	540	0.8	4.02	1.91	$-1.1{\cdot}10^{-6}$
FliteStrand SZT S-glass	Owens Corning	88	5.5	4.8–5.1	2.45	$2{\cdot}10^{-6}$
EC9 756 P109 E-glass	Owens Corning	72	4.5	3.5	2.56	$4.9{\cdot}10^{-6}$

α_{11} = Coefficient of thermal expansion in the axial direction

Table 2
Cured ply properties of the UD prepregs used in this study.

Prepreg Type	M55J /epoxy	S-glass/epoxy	E-glass/epoxy
Fibre mass per unit area [g/m^2]	30	190	192
Cured ply thickness [mm]	0.030	0.155	0.140
Fibre volume fraction [%]	52	51	54
Tensile strain to failure [%]	0.60[a]	3.98 [27], 3.56[b]	3.07[a]
Compressive strain to failure [%]	−0.31 [21]	−2.33[a]	–
Initial fibre direction elastic modulus, E_{11}[GPa]	280.0[b]	45.7 [27]	40.0[b]
Initial transverse direction elastic modulus, E_{22} [GPa]	6.2 [28]	15.4 [29]	15.4 [29]
Shear modulus, G_{12} [GPa]	5.0 [28]	4.34 [29]	4.34 [29]
Poisson's ratio ν_{12}	0.25 [28]	0.30 [29]	0.30 [29]
Manufacturer	North Thin-ply Technology	Hexcel	Hexcel

[a] Based-on manufacturer's data for 60% fibre volume fraction.
[b] Calculated for the given fibre volume fraction.

Table 3
UD hybrid composite specimen types examined under direct uniaxial compression.

Hybrid specimen	No. of carbon plies in one layer	Nominal single carbon layer thickness	Total no. of carbon plies	Nominal total carbon layer thickness	Measured total thickness
		[mm]		[mm]	[mm]
$[SG_1/(M55_1/SG_1)_{17}]$	1	0.03	17	0.51	3.30
$[SG_1/(M55_2/SG_1)_{17}]$	2	0.06	34	1.02	3.81
$[SG_1/(M55_3/SG_1)_{17}]$	3	0.09	51	1.53	4.32

SG stands for S-Glass/epoxy.
M55 stands for M55J carbon/epoxy.

2.3. Manufacturing method

The investigated UD hybrid laminates for the direct uniaxial compression testing and four-point bending were constructed from unidirectional plies in a temperature and humidity-controlled clean room. The finished laminates were placed inside a vacuum bag and cured inside an autoclave at the recommended cure temperature and pressure cycle for Hexcel 913 epoxy resin (60 min at 125 °C, 0.7 MPa). The resin and cure cycle were compatible with the other prepreg. The integrity of the hybrid laminates was confirmed during the mechanical testing. For the UD hybrid specimens examined under direct uniaxial compression loading, attaching end tabs using an adhesive was necessary to avoid premature failure in the gripping regions. End tabs of 1.6 mm thickness, made of glass/epoxy balanced fabric reinforced plates supplied by Heathcotes Co. Ltd., were bonded to the hybrid specimens using an Araldite 2014 type epoxy adhesive supplied by Huntsman and cured for 60 min at 70 °C inside a fan convection oven. The tabs and ends of the specimen were then ground flat to ensure good alignment and flat surfaces. The specimens were then fabricated using a diamond cutting wheel.

2.4. Mechanical test procedure

2.4.1. Direct uniaxial compression test

Uniaxial compression testing of the UD hybrid specimens was conducted under 1 mm/min displacement control on a computer-controlled Instron 600DX type 600 kN rated universal hydraulic test machine. Load and strain readings were logged onto a computer. Using the Imperial College loading rig, the specimens are supported laterally over the whole length of the tabs. Specimens were clamped lightly in position and then end-loaded between flat hardened plates. The high-precision clamping block and plate used in the rig minimise frictional effects

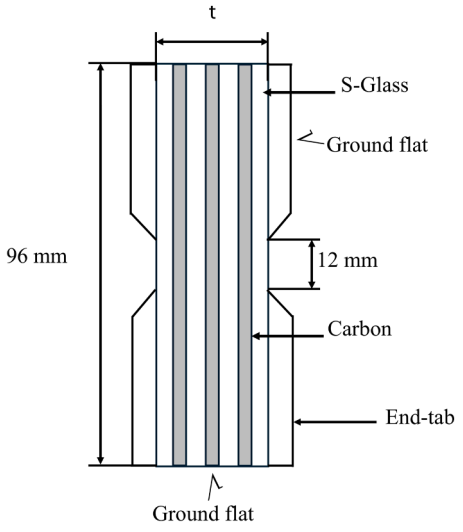

Fig. 1. The UD hybrid composite specimen's schematic shows the alternating lay-up sequence for uniaxial compression loading, where *t* is the nominal total thickness of the specimen.

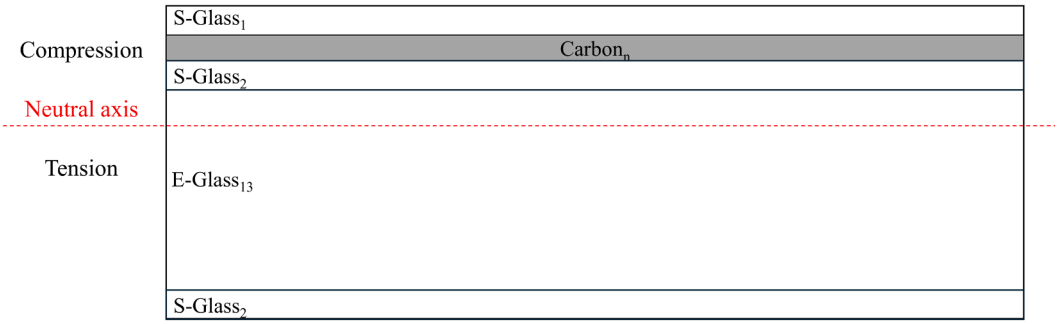

Fig. 2. Cross-sectional schematic of the asymmetric UD hybrid specimen showing the compression and tension region along with the approximate position of the neutral axis.

Table 4
Asymmetric hybrid specimen types tested under four-point bending.

Design	Lay-up sequence	Thickness (h) [mm]	Width (w) [mm]	Length (L) [mm]	Support span [mm]	Inner span [mm]	Loading nose diameter [mm]
Asym. $M55_n$	$[SG_2/EG_{13}/SG_2/M55_1/SG_1]$	2.63					
	$[SG_2/EG_{13}/SG_2/M55_2/SG_1]$	2.66	8	80	60	20	10
	$[SG_2/EG_{13}/SG_2/M55_3/SG_1]$	2.69					

SG stands for S-Glass/epoxy.
EG stands for E-Glass/epoxy.
M55 stands for M55J carbon/epoxy.

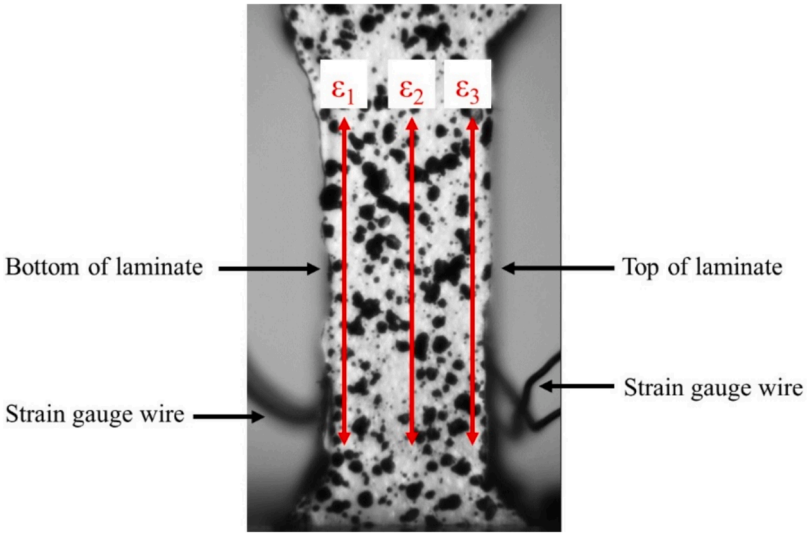

Fig. 3. Cut edge view of a direct uniaxial compression test setup with strain gauges attached to the top and bottom faces of the laminate prepared for the specimen. The speckle pattern on the edge is necessary for displacement tracking by the video gauge system.

and ensure combined axial and shear load introduction from the end and the sides, respectively.

Strain gauges of type C2A-06-062LW-120 from Micro-Measurements with the following dimensions: gauge length of 1.52 mm and 4.45 x 2.03 mm overall length and width, respectively, were used to measure the axial surface strain of the UD hybrid specimens. They were attached to the top and bottom surfaces of the tested laminate at the centre of the specimen's gauge length (see Fig. 3). The strain gauges were also used to detect any bending before fragmentation. An Imetrum video gauge system was also used to measure the axial strain of the specimens by tracking the applied speckle pattern on cut edges of the specimen, as shown in Fig. 3. Three strain measurements (ε_1, ε_2, ε_3) were made at different locations across the thickness of the specimens, as shown in Fig. 3. The approximate distance between each measurement probe is 1.60 mm. Those three measurements were made to ensure that the average axial compressive strain at the gauge length of the specimens is recorded. At least six specimens of each type were tested for direct uniaxial compression.

2.4.2. *Four-point bending test*

Four-point bending tests of the asymmetric UD hybrid specimens were carried out using a computer-controlled Instron 8872 type 25 kN rated universal hydraulic test machine with a 5 kN load cell. The tests were conducted under displacement control at a 1 mm/min crosshead speed. The four-point bending test setup is shown in Fig. 4. The support and inner spans were 60 mm and 20 mm, respectively. Reinforced rubber pads were placed between the loading noses and specimen contact surface to reduce the risk of local compressive failure of the surface glass layer under the inner loading noses.

The surface strains of the asymmetric UD hybrid specimens were

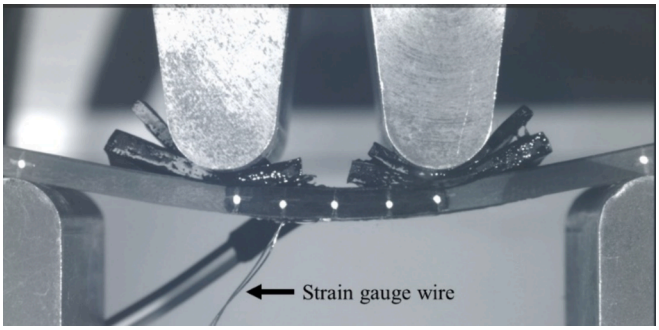

Fig. 4. Four-point bending test setup for an asymmetric UD hybrid composite specimen, with strain gauges attached to both sides of its surface.

measured using the same type of strain gauges utilized in the direct uniaxial compression test. White dots were added to the cut edge of the UD hybrid specimens, as shown in Fig. 4, to aid the video gauge in tracking the curvature of the specimens. The strain gauges were attached to the top and bottom faces (under compression and tension respectively) at the centre of the specimen's free length. As the strain gauges measure the surface strain of the S-GF/EP layer on the compression and tension sides, it was essential to calculate the strain at the top level of the CF/EP layer on the compression side. This was determined based on the linear variation of strain through the thickness by considering the distance from the neutral axis. At least six specimens of each type were tested under four-point bending.

3. Results and discussion

3.1. Direct uniaxial compression stress–strain response

The stress–strain curves shown in Figs. 5-7 were obtained from strain gauge recordings from both surfaces and the average of the video gauge strain readings from one cut edge of each UD hybrid specimen. As shown in Fig. 5, the strain gauge readings for a typical $[SG_1/(M55_1/SG_1)_{17}]$ specimen initially coincide but later show a slight deviation between the readings, indicating some bending, probably due to asymmetric damage development near the gauge. However, similar pseudo-yield-points (ε_{py}, σ_{py} visible as knee-points on the diagrams of Fig. 5 and Fig. 6) were recorded from all strain readings. The strain gauge reading at the top face of the $[SG_1/(M55_1/SG_1)_{17}]$ hybrid laminate shows a stress drop at about −1.7 % strain, indicating damage (delamination followed by buckling of the delaminated part) on that side, see Fig. 8. As the strain gauge was still attached despite the damage on the top face, it continued to measure the strain together with the strain gauge at the bottom face until the failure on both sides of the $[SG_1/(M55_1/SG_1)_{17}]$ specimen when the bottom face gauge stopped working. The video gauge strain for $[SG_1/(M55_1/SG_1)_{17}]$ shown in Fig. 5 was still available even after the damage on the top and bottom faces until the final failure of the hybrid laminate occurred.

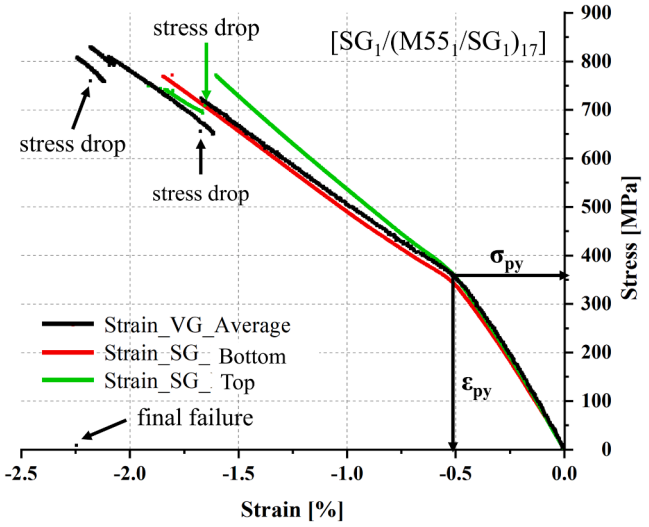

Fig. 5. The comparison of stress–strain curves from strain gauge and video gauge recordings for a typical $[SG_1/(M55_1/SG_1)_{17}]$ hybrid laminate suggests asymmetric damage after the pseudo-yield point.

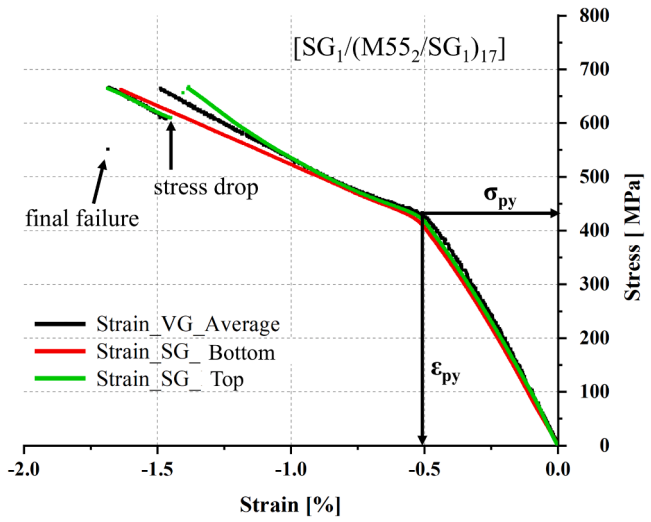

Fig. 6. The comparison of stress–strain curves from strain gauge and video gauge recordings for a typical $[SG_1/(M55_2/SG_1)_{17}]$ hybrid laminate suggests asymmetric damage after −1.0% strain.

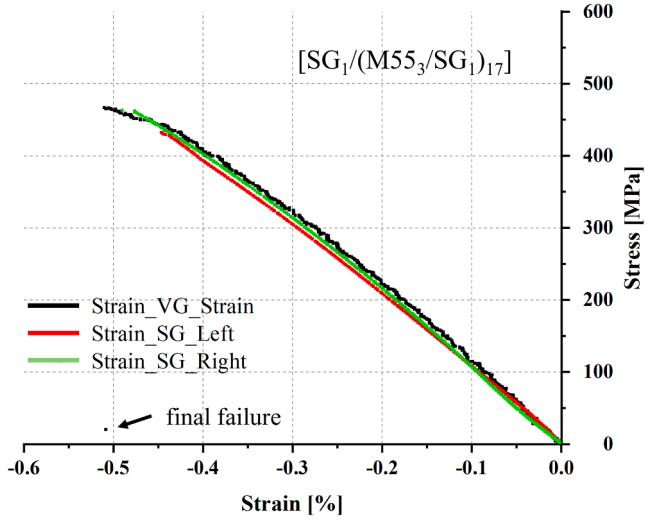

Fig. 7. The comparison of stress–strain curves from strain gauge and video gauge recordings for a typical $[SG_1/M55_3/SG_1)_{17}]$ hybrid laminate suggests no sign of bending before the final failure.

The strain gauge recording from both faces and the video gauge strain measurement of a typical $[SG_1/(M55_2/SG_1)_{17}]$ specimen coincides, as shown in Fig. 6, implying no sign of bending until well after the pseudo-yield point. A stress drop is apparent from the strain gauge at the top face and video gauge measurement after −1.0 % strain due to asymmetric damage to the $[SG_1/(M55_2/SG_1)_{17}]$ specimen. After the stress drop, the strain gauge at the top face of the $[SG_1/(M55_2/SG_1)_{17}]$ specimen was still attached to the damaged surface, thus able to measure

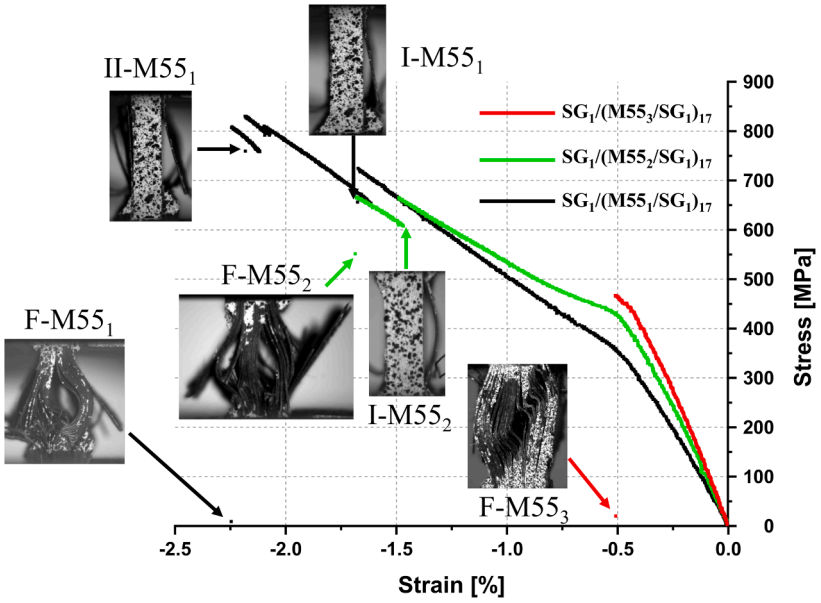

Fig. 8. Typical direct uniaxial compressive stress–strain curves for the three UD thin-ply hybrid composites with the damage mode for each hybrid. The notations I, II, and F refer to the first, second, and final stress drops for each UD thin-ply hybrid configuration.

the strain together with the strain gauge on the bottom face and the video gauge until the final failure of that hybrid specimen.

In the strain readings of a typical [SG$_1$/(M55$_3$/SG$_1$)$_{17}$] specimen, there is no sign of deviation between the readings from the strain gauges, which means no bending before the final stress drop when the strain gauges and video gauge stopped measuring due to complete failure of the specimen. The strain measurements from the strain gauges on both faces shown in Fig. 7 initially gave similar readings to the video gauge measurements until failure on the bottom and top faces occurred and the strain gauges stopped measuring. In contrast, the video gauge could continue the strain measurement until the hybrid specimen ultimately failed.

Because the video gauge can record the strain until the hybrid specimen's final failure, the strain from the video gauge measurement is reported as the compressive strain in the typical stress–strain curves for the hybrid composite laminates examined in direct uniaxial compression, shown in Fig. 8.

The overall compressive stress–strain responses show slight non-linearity even before the knee-points. The behaviour of the [SG$_1$/(M55$_1$/SG$_1$)$_{17}$] and [SG$_1$/(M55$_2$/SG$_1$)$_{17}$)] hybrids in Fig. 8 show smooth transitions between the initial non-linear part, followed by a short, slightly rising plateau and a final approximately linear increasing part. Only a slight non-linearity was observed for the [SG$_1$/(M55$_3$/SG$_1$)$_{17}$] hybrid, followed shortly by final failure. By incorporating more carbon plies into the hybrid laminates, the initial stiffness increases, as expected, which can be seen from the different initial slopes (E_i) of each stress–strain curve in Fig. 8, where the [SG$_1$/(M55$_3$/SG$_1$)$_{17}$] hybrid has the highest initial stiffness. As seen in Fig. 8, the first stress drops for [SG$_1$/(M55$_1$/SG$_1$)$_{17}$] occur at a higher strain compared to [SG$_1$/(M55$_2$/SG$_1$)$_{17}$]. The final stress drops for [SG$_1$/(M55$_1$/SG$_1$)$_{17}$] also occur at a higher strain than the other two hybrid configurations. The lowest final strain appears for [SG$_1$/(M55$_3$/SG$_1$)$_{17}$] as it has the thickest CF/EP layer. It is worth mentioning that the second stress drop only occur for the [SG$_1$/(M55$_1$/SG$_1$)$_{17}$] hybrid noted as II-M55$_1$ in Fig. 8. The stress drops at I and II were due to delamination at carbon-glass layer interfaces, causing detachment of sub-laminates (one CF/EP with the outermost GF/EP ply) on each side, followed by a compressive failure of the whole specimen at stage F, as depicted in Fig. 8.

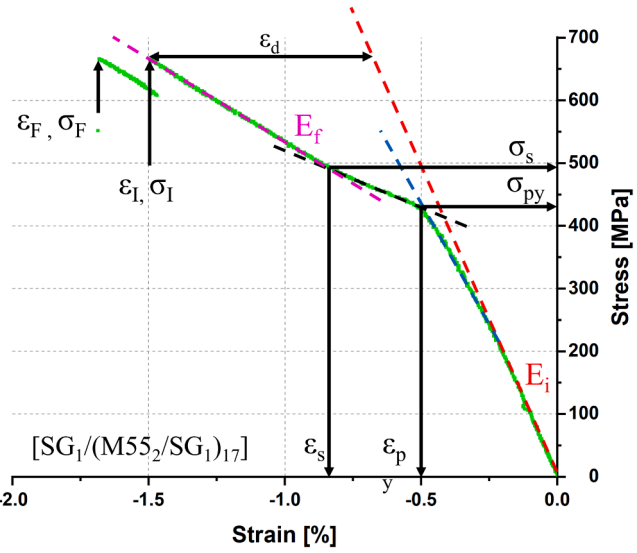

Fig. 9. The direct uniaxial compressive stress–strain curve displays the basic mechanical properties of UD thin-ply hybrid composites, where the initial stiffness (E_i) and final tangent stiffness (E_f), pseudo-yield point (ε_y and σ_y), fragmentation saturation point (ε_s and σ_s), first stress drop (ε_I and σ_I) and final stress drop points (ε_F and σ_F) are marked. The pseudo-ductile strain (ε_d) is defined as the difference between the strain at the first stress drop (ε_1) and the strain on the initial modulus line at the stress before the drop (σ_I).

The origin of the plateau in the compressive stress–strain curve is the progressive fragmentation and dispersed delamination, similar to the damage mechanisms in UD thin-ply hybrid composites with single and double carbon layers under tensile loading [2]. Due to the compressive loading, the plateau's slope in the compressive stress–strain curve is steeper than in the tensile stress–strain curve. The nature of compressive loading enables load transfer between carbon layer fragments across fracture surfaces, increasing the stress upon further compressive strain introduction. The method to determine the basic mechanical properties

Table 5
Mechanical properties of hybrid composites under direct compressive loading (numbers in brackets indicate coefficients of variation in [%]). The measured strains are corrected by adding the compressive thermal residual strain in the carbon layer. The thermal residual strains are −0.022%, −0.014% and −0.011 % for $[SG_1/(M55_1/SG_1)_{17}]$, $[SG_1/(M55_2/SG_1)_{17}]$, and $[SG_1/(M55_3/SG_1)_{17}]$ respectively.

	Design	$[SG_1/(M55_1/SG_1)_{17}]$	$[SG_1/(M55_2/SG_1)_{17}]$	$[SG_1/(M55_3/SG_1)_{17}]$
Properties	Description			
E_i [GPa]	Initial modulus	73.2 (2.9)	95.4 (5.8)	114.9 (2.4)
ε_{py} [%]	Pseudo-yield strain	−0.52 (3.2)	−0.51 (3.8)	–
σ_{py} [MPa]	Pseudo-yield stress	344 (3.6)	429 (1.0)	–
ε_s [%]	Saturation strain	–	−0.83 (4.0)	–
σ_s [MPa]	Saturation stress	–	484 (2.0)	–
ε_d [%]	Pseudo-ductile strain	−0.71 (13.4)	−0.70 (15.6)	–
E_f [GPa]	Final tangent modulus	33.1 (13.5)	23.2 (8.4)	–
ε_I [%]	First strain drop	−1.69 (10.9)	−1.21 (8.1)	–
σ_I [MPa]	First stress drop	697 (7.4)	574 (9.2)	–
ε_F [%]	Final strain drop	−2.15 (8.1)	−1.44 (8.7)	−0.50 (6.9)
σ_F[MPa]	Final stress drop	748 (5.8)	601 (6.9)	452 (8.0)

of the UD thin-ply hybrid composites under direct uniaxial compressive loading is illustrated in Fig. 9 and summarised in Table 5. The method in Fig. 9 is shown for the $[SG_1/(M55_2/SG_1)_{17}]$ hybrid; it also applies to the other two hybrids.

The initial stiffness of all hybrid composites was determined by measuring the slope of each specimen's response (see Fig. 9). The stress–strain curves for $[SG_1/(M55_1/SG_1)_{17}]$ and $[SG_1/(M55_2/SG_1)_{17})]$ hybrids exhibit four stages. In the initial loading stage, there is already non-linear behaviour due to the characteristics of the carbon fibres [31], causing a modulus reduction in the hybrid composite, deviating gradually from the initial linear red dashed line. Montagnier et al. [21] reported a compressive failure strain of around −0.31 % for the pure M55J carbon fibre composite with Structil R368-1 matrix, and it is suggested that the source of non-linearity starting from around −0.31 % up to the pseudo-yield point for the current hybrid configuration is due to the combined effect of the fracturing of a few carbon fibres and the intrinsic non-linearity of the carbon fibres. In the hybrid composites, the fracturing of the carbon fibres did not result in sudden failure because of the support of the adjacent S-GF/EP plies; in contrast, in the pure M55J carbon fibre composite, according to the authors [21], fibre fractures lead immediately to complete failure which could be attributed to the absence of support from the high-strain S-GF/EP layer.

The non-linearity increases with strain until it reaches the pseudo-yield point, determined from the intersection of the dashed blue and black lines, respectively (see Fig. 9). From the pseudo-yield point, a process of multiple carbon layer fragmentation and dispersed delamination occurs, resulting in further stiffness reduction and non-linearity shown as the change of slope on the $[SG_1/(M55_1/SG_1)_{17}]$ and $[SG_1/(M55_2/SG_1)_{17})]$ stress–strain curves. A closer examination of the compressive stress–strain curves in Fig. 8 shows that the change of slope is more distinctive for the $[SG_1/(M55_2/SG_1)_{17})]$ hybrid compared to the $[SG_1/(M55_1/SG_1)_{17}]$ hybrid due to the higher ratio of fragmenting carbon plies causing a more significant stiffness loss for the $[SG_1/(M55_2/SG_1)_{17})]$ hybrid. The progressive fragmentation developed gradually upon further loading, reaching the saturation point (see Fig. 9.). The stress–strain curves of the $[SG_1/(M55_1/SG_1)_{17})]$ and $[SG_1/(M55_3/SG_1)_{17})]$ hybrids in Fig. 8 show that a saturation point is not apparent; thus, only the saturation point for $[SG_1/(M55_2/SG_1)_{17})]$ is reported in Table 5. Beyond the fragmentation saturation point, the additional load is mostly carried by the intact GF/EP layers, and the stress rises further until it reaches the first stress drop point (ε_I, σ_I) (see Fig. 9). The tangent stiffness of this section is evaluated as E_f. In contrast, the actual stiffness of the coupons at a given damaged state is best represented by a line between the origin and the final point of the stress–strain curve (secant or unloading modulus), as there are intact load-bearing elements (i.e. the GF/EP layers) in the coupons until the final failure.

For the $[SG_1/(M55_3/SG_1)_{17}]$ hybrid, some nonlinearity was observed before sudden final failure occurred at around −0.50 % strain. We attribute this effect mainly to the nonlinearity of the carbon fibres. This lower final failure strain is still significantly higher than the reported compressive strain at failure of −0.31 % for the same M55J fibres with Structil R368-1 matrix [21] due to the constraining effect of the adjacent S-GF/EP plies on the failure of the CF/EP layers.

The measured compressive strains were corrected by adding the calculated compressive thermal residual elastic strain in the carbon layer to yield the actual elastic strains, as shown in Table 5. The compressive thermal residual elastic strain in the carbon layer (ε_{el}) was determined from the unconstrained thermal strain $\varepsilon_{thermal}$ as follows:

$$\varepsilon_{el} = \varepsilon_{total} - \varepsilon_{thermal} \tag{1}$$

$$\varepsilon_{thermal} = \alpha_{hybrid}\Delta T \tag{2}$$

The coefficient of thermal expansion (CTE) of the UD hybrid composite (α_{hybrid}) is calculated by taking into account the elastic properties of the CF/EP and GF/EP layers given in Table 1 and Table 2 and their CTE's in the axial direction (α_{11}) as follows:

$$\alpha_{hybrid} = \frac{t_{CF/EP}}{t_{hybrid}}\cdot\alpha_{11(CF/EP)}\cdot\frac{E_{CF/EP}}{E_{hybrid}} + \left(1 - \frac{t_{CF/EP}}{t_{hybrid}}\right)\cdot\alpha_{11(GF/EP)}\cdot\frac{E_{GF/EP}}{E_{hybrid}} \tag{3}$$

Where $t_{CF/EP}$, t_{hybrid}, $\alpha_{11(CF/EP)}$, $E_{CF/EP}$, E_{hybrid}, $\alpha_{11(GF/EP)}$, $E_{GF/EP}$ are the thickness of M55J carbon/epoxy layer, total thickness of the UD hybrid layer, CTE of M55J carbon/epoxy layer, initial modulus of M55J carbon/epoxy layer, initial modulus of the UD hybrid layer, CTE of S-Glass/epoxy layer, initial modulus of S-Glass/epoxy layer. The initial modulus of the UD hybrid layer is calculated by using the equation to calculate initial equivalent modulus as shown in [9]. For the asymmetric hybrid specimen, $E_{GF/EP}$ is calculated based on the rule of mixtures, and takes the relative stiffness and thickness of S-Glass/epoxy and E-Glass/epoxy layers respectively. The total strain (ε_{total}) was measured directly during the test. The temperature difference (ΔT) from the cure temperature to room temperature in Equation (2) is assumed as 100 °C. The fragmentation strain at the pseudo-yield point in this work is similar to the strain reported by Wu et al. [28] for their $[\pm 27_7/0]_s$ hybrid configuration. It should be noted that the thermal residual strain is −0.03 % for the angle ply configuration [28] which is higher than that for the unidirectional thin-ply hybrid composites examined under direct compression in this work (i.e. −0.022 %, −0.014 % and −0.011 % for the three different configurations).

Table 5 shows that with increasing number of carbon plies incorporated in the hybrid laminates, the strain at first stress drop (ε_I) and final failure strain (ε_F) decrease. The pseudo-yield strain for $[SG_1/(M55_1/SG_1)_{17}]$ and $[SG_1/(M55_2/SG_1)_{17}]$, as seen in Table 5, is similar. No pseudo-yield strain was observed for the $[SG_1/(M55_3/SG_1)_{17}]$ hybrid because the hybrid laminates suddenly failed at −0.5 % as shown in Table 5. The graphic illustrating the relation between ε_{py}, ε_I, and ε_F with increasing carbon layer thickness for all three hybrids is given in Fig. 10.

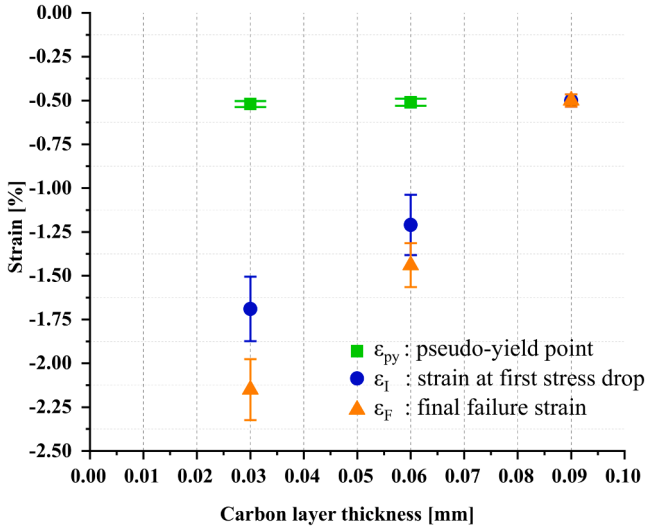

Fig. 10. The pseudo-yield strain (ε_{py}), strain at first stress drop (ε_I), and final failure strain (ε_F) as a function of the carbon layer thickness. With increasing carbon layer thickness, the strains ε_I and ε_F are lower, and for ($[SG_1/(M55_3/SG_1)_{17}]$), there is no ε_{py}.

The different values for ε_I and ε_F shown in Fig. 10 are due to the different energy release rates for delamination after fracturing of the carbon plies in each hybrid. As the energy release rates are approximately proportional to the thickness of the carbon layer, delamination occurs at a lower strain for the hybrid with double carbon plies ($[SG_1/(M55_2/SG_1)_{17}]$) compared with the single carbon ply case ($[SG_1/(M55_1/SG_1)_{17}]$). For the hybrid with triple carbon plies ($[SG_1/(M55_3/SG_1)_{17}]$), there is no pseudo-yield strain (ε_{py}), as shown in Fig. 10, due to immediate delamination after the carbon layer fractures, as it has the highest energy release rates.

3.2. Four-point bending response

Typical force-strain responses for the three asymmetric hybrid composites under four-point bending are shown in Fig. 11 and the basic mechanical properties are shown in Table 6. The thermal residual strain for the asymmetric hybrids is calculated considering the entire laminate.

It is worth mentioning that the thermal residual strain for the asymmetric hybrids designed for the bending tests is higher than in case of the hybrid composite configurations for direct compression because the specimens are mainly composed of a thick E-glass/epoxy layer with higher CTE. As expected, the initial stiffness increases with more carbon plies in the hybrid laminates. An initial approximately linear elastic response is shown for all three hybrid composites, followed by a noticeable change in the slope after the pseudo-yield point (see Fig. 11a) for the asymmetric $M55_2$ and asymmetric $M55_3$, respectively. The pseudo-yield point is determined from the deviation of the green force-strain curve from the red dashed line, as shown in Fig. 11b for the asymmetric $M55_2$ hybrid force-strain curve. It was more challenging to assess the change in slope for the asymmetric $M55_1$ due to the small stiffness contribution of the single thin CF/EP ply.

The pseudo-yield point, which marks established fragmentation in the CF/EP ply, was followed by reduced stiffness and slope change corresponding to further progressive fragmentation and dispersed delamination between the CF/EP and S-GF/EP plies. Beyond the pseudo-yield point, further load is carried by the intact S-GF/EP plies, causing a continuous increase in load until the final failure due to delamination between the CF/EP and S-GF/EP layers. After fragmentation at the pseudo-yield point, the asymmetric hybrid laminate with the single, double, and triple CF/EP plies did not fail immediately because the load was transferred from the fractured CF/EP plies to the S-GF/EP plies which remained intact. The bulk of the asymmetric hybrid specimen is made of S-GF/EP and E-GF/EP plies, which were able to support the fractured CF/EP plies and thus delay the final failure until higher strain.

Table 6
Mechanical properties of asymmetric hybrid composites under four-point bending (numbers in brackets indicate coefficients of variation in [%]). The measured strains are corrected by adding the compressive thermal residual strain in the carbon layer. The thermal residual strains are −0.061%, −0.057%. and −0.053 % for asymmetric $M55_1$, asymmetric $M55_2$, and asymmetric $M55_3$ respectively.

	Design	Asym. $M55_1$	Asym. $M55_2$	Asym. $M55_3$
Properties	Description			
ε_{py} [%]	Pseudo-yield strain	−0.56 (2.2)	−0.53 (6.8)	−0.53 (2.6)
F_{py} [N]	Pseudo-yield force	279 (4.1)	292 (12.0)	364 (3.1)
ε_F [%]	Final failure strain	−2.73 (12.1)	−1.97 (9.0)	−1.24 (4.3)
F_F [N]	Final failure force	1527 (11.6)	1009 (11.3)	700 (6.9)

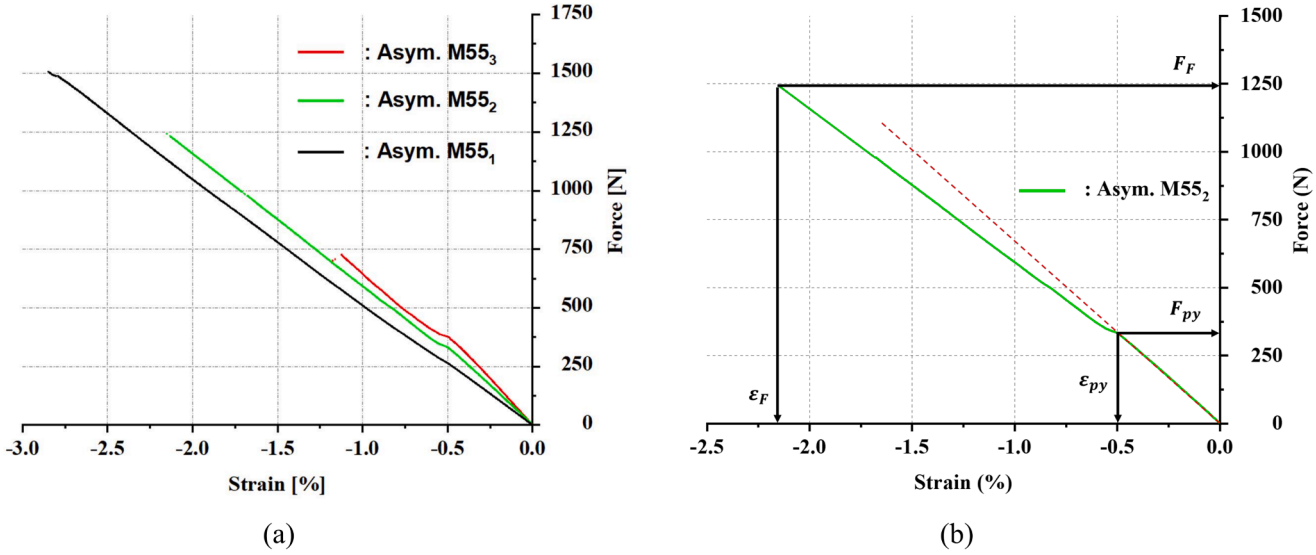

Fig. 11. (a) Typical force-strain curves for the three asymmetric hybrid composites, with the strains calculated for the top level of the carbon ply, (b) the method to determine the pseudo-yield point for the asymmetric $M55_2$ and the other two hybrids.

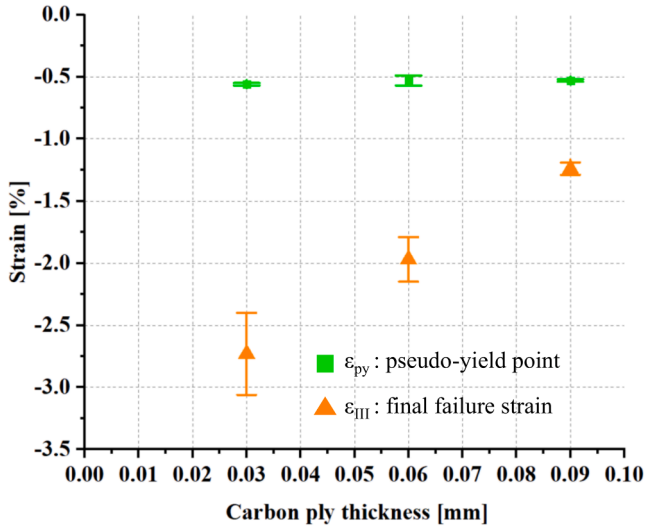

Fig. 12. The pseudo-yield strain (ε_{py}) and final failure strain (ε_F) in function of the carbon layer thickness.

The final failure of the asymmetric hybrid composites occurs at different compressive strains due to different energy release rates related to the thickness of CF/EP layer.

The plateaus in the load–strain curves for asymmetric $M55_2$ and asymmetric $M55_3$, shown in Fig. 11, are less distinctive than the plateaus observed under direct compression due to the lower ratio of fragmenting CF/EP layers and since only the CF/EP layers on the compression side of the asymmetric hybrids fragmented.

Fig. 12 illustrates the relation between ε_{py} and ε_F with increasing carbon layer thickness for the asymmetric hybrid composites. It is shown that with increasing total carbon layer thickness, the final failure strain (ε_F) decreases, but the pseudo-yield strains (ε_{py}) are similar.

The different values for ε_F shown in Fig. 12 are due to the different energy release rates for delamination after the carbon layer in each hybrid is fractured. As the energy release rates are proportional to the thickness of the carbon layer [9 2], delamination occurs at a lower strain for the hybrid with double and triple CF/EP plies compared to the hybrid with single CF/EP ply.

3.3. Damage and failure mechanisms under direct uniaxial compressive loading and four-point bending

Visual investigation on the $[SG_1/(M55_1/SG_1)_{17}]$ and $[SG_1/(M55_2/SG_1)_{17}]$ hybrids, which have been loaded until −0.80 %, near the saturation point under direct compression, shows an irregular striped pattern where light areas are signs of localised delaminations surrounding the carbon layer fractures (see Fig. 13). The damage pattern of asymmetric hybrid specimen is similar, and is shown in Appendix C. The irregularity of the striped pattern shown is due to the variability in the carbon layer thickness, where the thicker parts tend to produce larger delamination areas. As shown in Fig. 13a, the $[SG_1/(M55_1/SG_1)_{17}]$ hybrid developed a denser striped pattern, which is likely a sign of the shorter fragment length. The $[SG_1/(M55_2/SG_1)_{17}]$ hybrid has a striped pattern that is more obvious and less dense than that of the $[SG_1/(M55_1/SG_1)_{17}]$ hybrid because of its longer fragment length. The delamination pattern in both hybrids was easily observed due to the translucent nature of the outer S-GF/EP layer. The damage pattern of both hybrids under compression is similar to the damage pattern of UD thin-ply hybrid composites with different thickness CF/EP layers under tensile loading [2,9].

As seen in Fig. 13a **and** Fig. 13b, the fragmentation and delamination area density changes with the thickness of the CF/EP layer. The striped pattern was not observed on the $[SG_1/(M55_3/SG_1)_{17}]$ hybrid, instead an extensive bright area corresponding to delamination and longitudinal ply splitting corresponding to final failure around −0.50 % strain was observed, as shown in Fig. 13c. Due to the higher energy release rate for the $[SG_1/(M55_3/SG_1)_{17}]$ hybrid, immediate delamination occurred around the initial carbon layer fracture.

The polished edge of the $[SG_1/(M55_2/SG_1)_{17}]$ hybrid shown in Fig. 14 shows fragmentation of the carbon layer across its thickness. The damage pattern of $[SG_1/(M55_1/SG_1)_{17}]$ is similar, and is shown in Appendix B. The carbon layers in both cases were broken into pieces around or shorter than one mm along the specimen's length under direct compressive loading once the M55J carbon layers reached their fracture strain. It is also shown that the fractures in the carbon layers developed at an angle of approximately 45° (see Fig. 14). For the single and double carbon ply cases $[SG_1/(M55_1/SG_1)_{17}]$ and $[SG_1/(M55_2/SG_1)_{17}]$ hybrids at −0.80 %, no fully developed delamination was observed because they have not reached the final failure point yet.

For the $[SG_1/(M55_3/SG_1)_{17}]$ hybrid shown in Fig. 15 fractured carbon layers and large scale delaminations are seen at the final failure of the specimen. Dobb et al. [32] reported failure of single high-modulus carbon fibres at an angle of approximately 45° due to instability at the fibre level, which leads to what looks like a shear fracture. It is possible that a similar mechanism might also be responsible for the shear fracture appearance of the M55J carbon layer under direct compressive loading, as shown in Fig. 14.

A previously tested asymmetric $M55_2$ hybrid specimen was inserted into a loading frame resembling the test machine's four-point bending

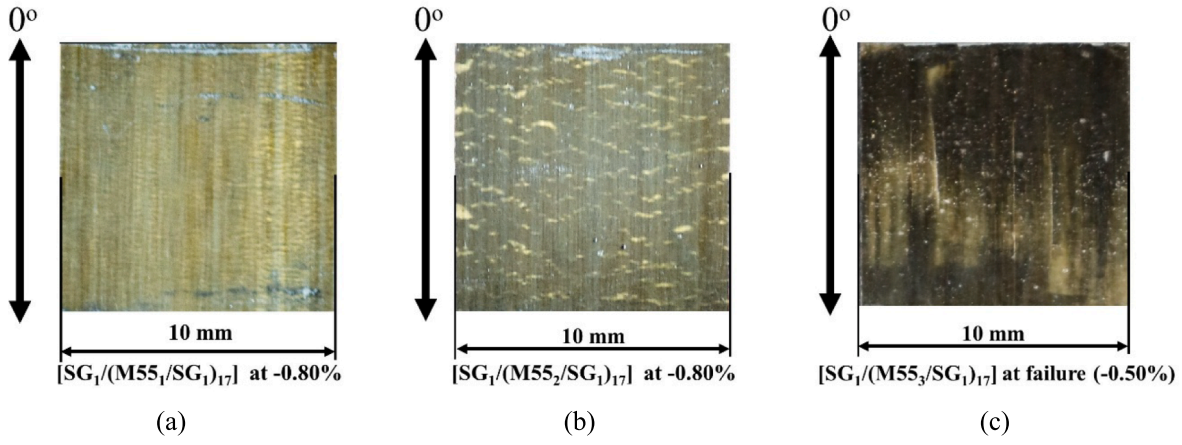

Fig. 13. Damage appearance on the surface of different hybrid laminates under direct uniaxial compression loading, with the arrows showing the 0° fibre direction. Images on (a) and (b) are taken after interrupted tests and on (c) after failure.

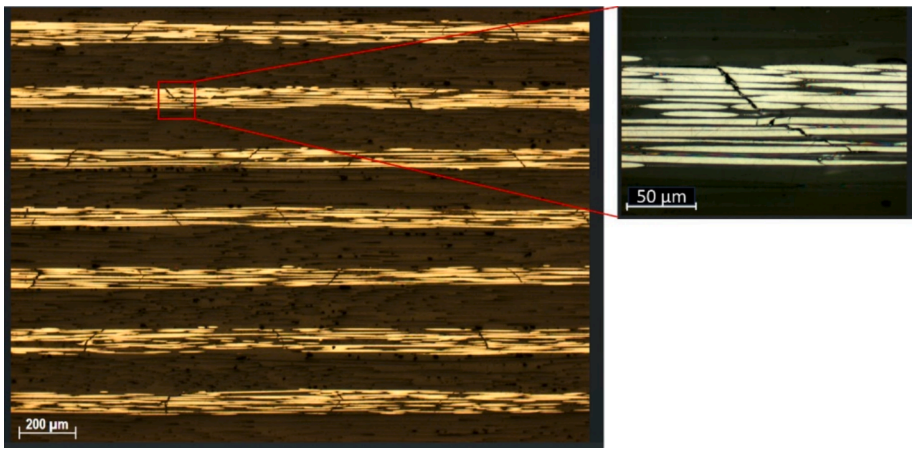

Fig. 14. Typical damage pattern of $[SG_1/(M55_2/SG_1)_{17}]$ after loading until −0.80% compressive strain, showing fragmentation of the carbon/epoxy layers and the intact glass/epoxy layers.

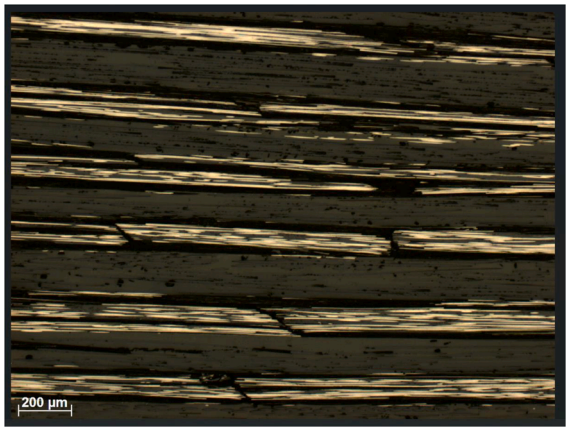

Fig. 15. Damage pattern of $[SG_1/(M55_3/SG_1)_{17}]$ after failure, showing carbon layer fractures, delaminations within the carbon layers, delaminations between glass and carbon layers.

fixture to study the damage interaction between the fragmented carbon layer and delamination in the hybrid composites under compressive loading. The device reloaded the specimens and assisted in opening the cracks under the optical microscope. The damage mechanism observed from the edge of the asymmetric $M55_2$ hybrid is shown in Fig. 16.

Fig. 16a shows that the carbon ply is fragmented at an angle (θ) of approximately 45° to the fibre direction. When loaded to approximately −1.4 % strain, as shown in Fig. 16b, the fragmented CF/EP ply is displaced in the out-of-plane direction, causing local interfacial damage (delamination). An examination of the same asymmetric $M55_2$ under scanning electron microscopy (SEM) in Fig. 17 shows a fractured CF/EP layer and clear local delamination areas between the CF/EP and GF/EP layers. It should be noted that the same loading frame was used to examine the asymmetric hybrid specimen under SEM.

The CF/EP layer displacement in the out-of-plane direction is possible because of the hybrid composites' low transverse modulus (E_{33}) and local delamination at the tip of the fractured area between the S-GF/EP and CF/EP layers. The displacement in the thickness direction (wedging action) is the reason for local delamination between the layers at the opening regions. The local delamination appears as the bright striped pattern shown in Fig. 13a **and** Fig. 13b. A schematic of the postulated compressive damage mechanisms in the UD thin-ply hybrid composites under compression is shown in Fig. 18. A combination of fragmentation, wedging action and local delamination is responsible for the stiffness loss and pseudo-ductile strain.

Because the carbon layer fractures into smaller pieces, the distances between the fractures (i.e., the carbon layer fragment lengths) can be assessed by measuring the distances between the stripes in the patterns. The measurement was done at several intervals across the width of the specimen since the stripes are not entirely straight and are irregularly spaced, as shown in Fig. 19 for the $[SG_1/(M55_2/SG_1)_{17}]$ case. The distance between the bright stripes, seen from the surface, was measured because the stripes indicate the fracture lines in the CF/EP layer. The same method was used to measure the fragment lengths for $[SG_1/(M55_1/SG_1)_{17}]$ tested under direct compression and the asymmetric

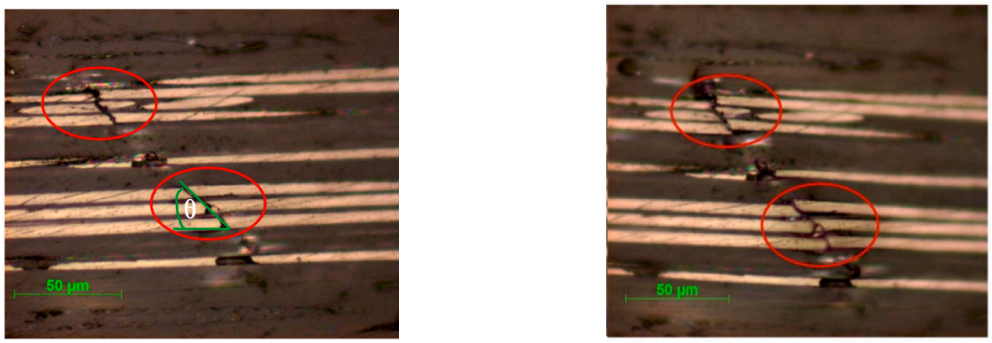

(a) (b)

Fig. 16. Damage mechanisms of asymmetric $M55_2$ hybrid: **(a)** unloaded state: fragmented carbon layer and ≈ 45° fragmentation angle (θ), unloaded **(b)** at −1.4% strain: fragmentation and wedging action.

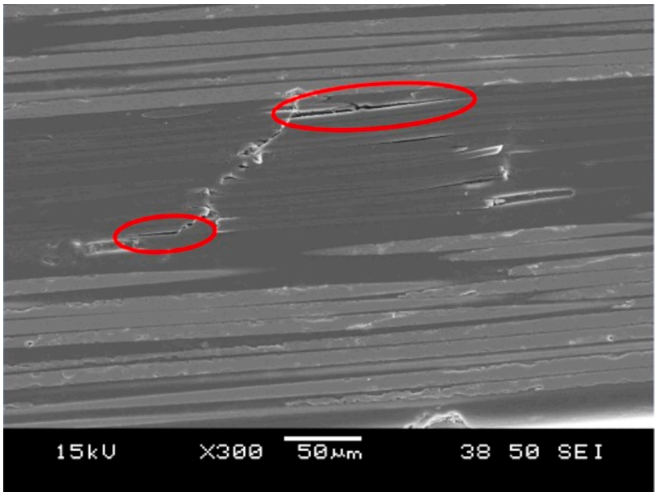

Fig. 17. Scanning electron microscopy examination of the interaction between CF/EP layer fragmentation and delamination for the asymmetric $M55_2$ hybrid composite under approximately −1.2% strain. The red ovals highlight local delaminations. (For interpretation of the references to colour in this figure legend, the reader is referred to the web version of this article.)

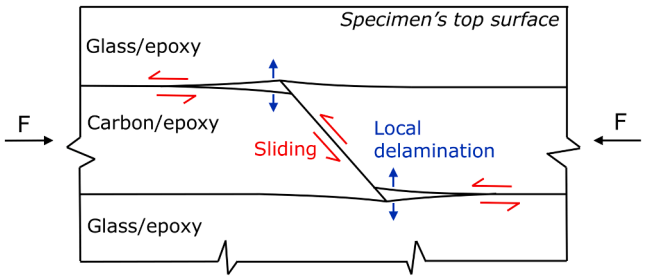

Fig. 18. Schematic of the postulated damage mechanisms in UD thin-ply hybrid composites under compression through direct compression and bending. A combination of fragmentation and wedging action is shown.

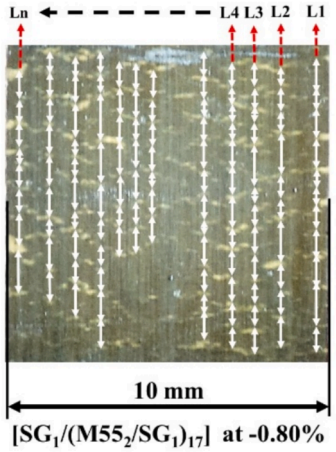

Fig. 19. An example of visual damage observation showing an irregular striped pattern at −0.80% strain and the method to measure the distance between carbon layer fractures in $[SG_1/(M55_2/SG_1)_{17}]$ hybrid. The notation L stands for the line number at each measurement.

hybrid composites tested under bending. In the case of the asym. $M55_1$ specimen type, fractures of the CF/EP layer were detected from the polished view of the specimen edges.

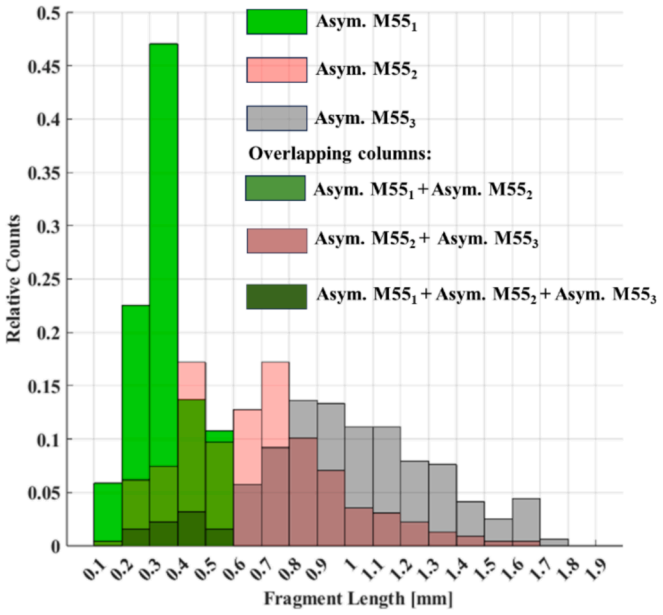

Fig. 20. Distribution of the fragment lengths after applying −0.80 % strain to the asymmetric hybrid composites in 4-point bending. Overlapping histograms are described by the notation Asym. $M55_n$ + Asym. $M55_{n+1}$, where n is the number of CF/EP plies in one layer.

Table 7
Average fragment length and the estimated critical fragment length of UD hybrid composites under direct compression and bending testing.

The number of CF/EP plies in one layer	Nominal thickness of CF/EP layer [mm]	Average fragment length [mm]		Estimated critical fragment length in tension [mm]
		Direct compression	Bending	
1	0.03	0.31	0.35	0.50
2	0.06	0.48	0.68	1.05
3	0.09	–	1.01	1.60

The fragment length measurements from the asymmetric hybrid specimens are shown in Fig. 20, and similar results from direct compression are given in Appendix B. Fig. 20 shows that the average fragment length increases with thicker CF/EP layers in the laminates. After reaching the compressive failure strain, the CF/EP layer fractures into fragments but still sustains some load. As the thickness of the CF/EP layer increases, a longer shear stress transfer zone length is formed increasing the resulting average fragment length.

The average fragment lengths of the UD hybrid composites from both direct compression and bending testing and the estimated critical fragment length is shown in Table 7.

For tensile loading, a critical ply length, Lc, can be defined as the minimum length required to achieve full reintroduction of load by shear in a fractured ply. A similar approach was applied here to understand the load transfer mechanism and to examine if any critical ply length exists in the present hybrid composites under direct compression and four-point bending. The critical fragment length was determined using the Kelly-Tyson type equation, $L_c = \frac{E_c \cdot \varepsilon_c \cdot t_c}{\tau_{max}}$ in [27,33] where Ec, ε_c, t_c are Young's modulus of the CF/EP ply, compressive failure strain of the CF/EP ply at the pseudo-yield point taken as 0.50 %, and thickness of the CF/EP ply respectively. Assuming linear elastic-perfectly plastic response in the matrix with constant shear stress and τ_{max} of 77.6 MPa [34] as the interfacial shear stress at the S-GF/EP and CF/EP composite interfaces, the obtained estimated critical fragment lengths are shown in

Table 7.

The mean fragment lengths of the hybrid composites observed under direct compression and four-point bending are shorter than the estimated critical fragment length based on the formula developed for tension loading. This is expected, as the load transfer mechanisms in tension and compression are different. The contact between the fragments under compressive loading allows load to be transferred between the fragments in the CF/EP layer after fragmentation (unlike under tensile load), reducing the required shear load transfer length and allowing shorter mean lengths of the fragments.

3.4. Comparison between uniaxial direct compression and four-point bending test results

The comparison between characteristic strains obtained from direct compression and bending tests is shown in Table 8. It is worth mentioning that determining the pseudo-yield point is much harder in four-point bending compared to direct compression, especially for the single ply case, which means that caution is needed when reading the strains from the bending test. The strains were corrected by adding the calculated compressive thermal residual strain in the carbon layer to yield the actual elastic strains.

It has previously been shown that compressive strains at shear instability failure are higher in carbon layers loaded in bending due to the strain gradient through the thickness as shown by Wisnom et al. [24]. The ε_{py} of hybrid specimens obtained from compression and four-point bending tests are similar, as expected since fragmentation is associated with fibre failure, not instability at the composite level. The similar strains for different carbon to glass volume ratios show that the varying degrees of support from the glass layers does not significantly affect the carbon failure strain, as expected for fibre fracture dominated failure. Four-point bending tests on a thin monolithic M55J carbon/cyanate ester beam laminates with different thicknesses also showed no kink-bands after the specimen failed [35], consistent with the present results.

The final failure (ε_F) strains in Table 8 obtained from bending tests are higher than those from direct compression testing. This is believed to be due to the higher energy release rate for the hybrid composites under axial compressive loading than in bending. Analytical work by Petrossian et al. [36] has shown that the energy release rate for delamination from cut unidirectional plies in axial loading is higher than in bending due to the strain gradient in bending. This also explains how a knee-point could be obtained for the three-carbon ply case in bending, whereas in direct compression the specimens failed around that point.

4. Conclusions

This paper has presented the mechanical properties and damage mechanisms of unidirectional hybrid composites of thin M55J high modulus carbon and standard thickness S-glass layers subjected to compressive and four-point bending loading. The effect of the different numbers of carbon plies in the carbon layers and different ratios between the total thickness of the carbon and glass layers was examined. The following conclusions were drawn:

- Pseudo-ductile response in uniaxial direct compression has been demonstrated. Gradual failure with a significant decrease in stiffness at around −0.50 % strain and final failure at −2.15 % and −1.44 % strain have been obtained for the $[SG_1/(M55_1/SG_1)_{17}]$ and $[SG_1/(M55_2/SG_1)_{17}]$ hybrid configurations, respectively.
- For the $[SG_1/(M55_3/SG_1)_{17}]$ hybrid, sudden failure occurred at around −0.50 % strain in direct compression. This lower strain is still significantly higher than the compressive strain at failure of −0.31 % for the same M55J fibres but different/ Structil R368-1 matrix, as reported by Montagnier et al. [21].

Table 8
Pseudo-yield and final failure strain comparison between uniaxial direct compression and four-point bending testing (numbers in brackets indicate the coefficient of variation [relative %]). The measured strains are corrected by the compressive thermal residual strain in the carbon layer.

The number of CF/EP plies in one layer	Nominal thickness of CF/EP layer [mm]	Pseudo-yield strain (ε_{py}) [%]		Final failure strain (ε_F) [%]	
		Direct compression	Bending	Direct compression	Bending
1	0.03	−0.52 (3.2)	−0.56 (2.2)	−2.15 (8.1)	−2.73 (12.1)
2	0.06	−0.51 (3.8)	−0.53 (6.8)	−1.44 (8.7)	−1.97 (9.0)
3	0.09	–	−0.53 (2.6)	−0.50 (6.9)	−1.24 (4.3)

- The behaviour of UD thin-ply hybrid composites under direct compression and 4 point bending can be described by the following damage mechanism sequence: 1. Quasi-elastic phase: early non-linearity due to the combined effect of intrinsic carbon fibre behaviour and a few carbon fibre fractures, 2. Fragmentation phase: fragmentation of the carbon layer with stable localised delaminations between the carbon and glass layers at carbon layer fractures, and 3. Final failure due to large-scale delamination of the carbon layers.
- The load transfer mechanism within the damaged carbon layers in compression is not the same as in the tension case, as shown by the shorter carbon layer fragment length compared to the calculated critical length in the tension case. In compression, contact between the fragments is maintained, enabling continued load carrying and further fracture into smaller lengths upon further deformation.
- When the hybrids are loaded in four-point bending, the final failure strain due to delamination is higher compared to the final delamination strain in direct compression due to the lower energy release rate in bending.
- The similarity of the pseudo-yield point strain obtained from direct compression and bending tests indicates that fragmentation at that point is due to carbon fibre failure, not instability at the composite layer level. The pseudo-yield strain is also not affected by the volume ratio of carbon to glass plies provided that premature delamination does not occur.
- The factor that governs the final failure of the UD thin-ply hybrid composites under compression is the thickness of the high-modulus carbon layers. This controls the final failure strain due to delamination, which decreases with an increasing carbon layer thickness.

CRediT authorship contribution statement

Putu Suwarta: Writing – original draft, Visualization, Methodology, Investigation, Conceptualization. **Michael R. Wisnom:** Writing – review & editing, Supervision, Resources, Methodology, Investigation, Funding acquisition, Conceptualization. **Mohamad Fotouhi:** Writing – review & editing, Methodology, Investigation. **Xun Wu:** Writing – review & editing, Methodology, Investigation. **Gergely Czel:** Writing – review & editing, Supervision, Methodology, Conceptualization.

Declaration of competing interest

The authors declare the following financial interests/personal relationships which may be considered as potential competing interests: [Michael R. Wisnom reports financial support was provided by UK Engineering and Physical Sciences Research Council. Putu Suwarta reports financial support was provided by The Directorate General of Higher Education of the Ministry of Education and Culture of the Republic of Indonesia (DIKTI). Putu Suwarta reports financial support was provided

by Indonesia Endowment Fund for Education (LPDP). Gergely Czel reports financial support was provided by National Research, Development and Innovation Office (NRDI, Hungary). Gergely Czel reports financial support was provided by Ministry of Culture and Innovation of Hungary. Gergely Czel reports financial support was provided by Hungarian Academy of Sciences. If there are other authors, they declare that they have no known competing financial interests or personal relationships that could have appeared to influence the work reported in this paper].

Acknowledgement

This work was funded under the UK Engineering and Physical Sciences Research Council Programme Grant EP/I02946X/1 on High-Performance Ductile Composite Technology in collaboration with Imperial College, London. Putu Suwarta acknowledges The Directorate General of Higher Education of the Ministry of Education and Culture of the Republic of Indonesia (DIKTI) for funding through the DIKTI scholarship. Putu Suwarta acknowledges Thomas Pozegic for checking the writing and grammar in this paper. He also acknowledges the support from Indonesia Endowment Fund for Education (LPDP) through Higher Education Endowment Fund (DAPT) Program 2023/2024. Gergely Czél acknowledges the National Research, Development and Innovation Office (NRDI, Hungary) for support through grant OTKA FK 131882, and the Ministry of Culture and Innovation of Hungary for support from the National Research, Development and Innovation Fund through grant no. NKKP ADVANCED 149578 and under the TKP2021-NVA funding scheme through grant no. TKP-6-6/PALY-2021 and from the Complex Development funding scheme through grant no. 2022-2.1.1-NL- 2022-00012 Creation of National Laboratories. He is also grateful for support through the János Bolyai Research Scholarship of the Hungarian Academy of Sciences.

Appendix A. The method to determine the pseudo-yield point for the asymmetric hybrid composites

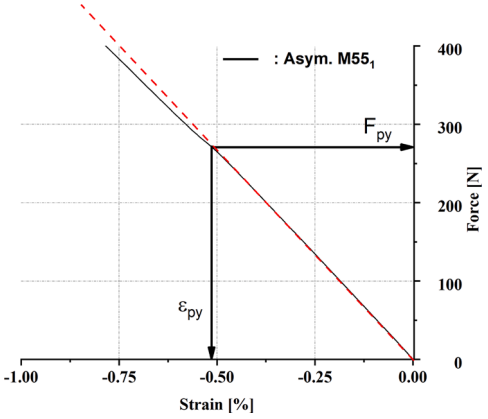

Fig. A1. Typical load–strain curve for an asymmetric $M55_1$ hybrid composite showing the pseudo-yield point determined from deviation of red dashed line from black force-strain curve.

Appendix B. Damage pattern of the unidirectional thin-ply hybrid composites under uniaxial compression loading

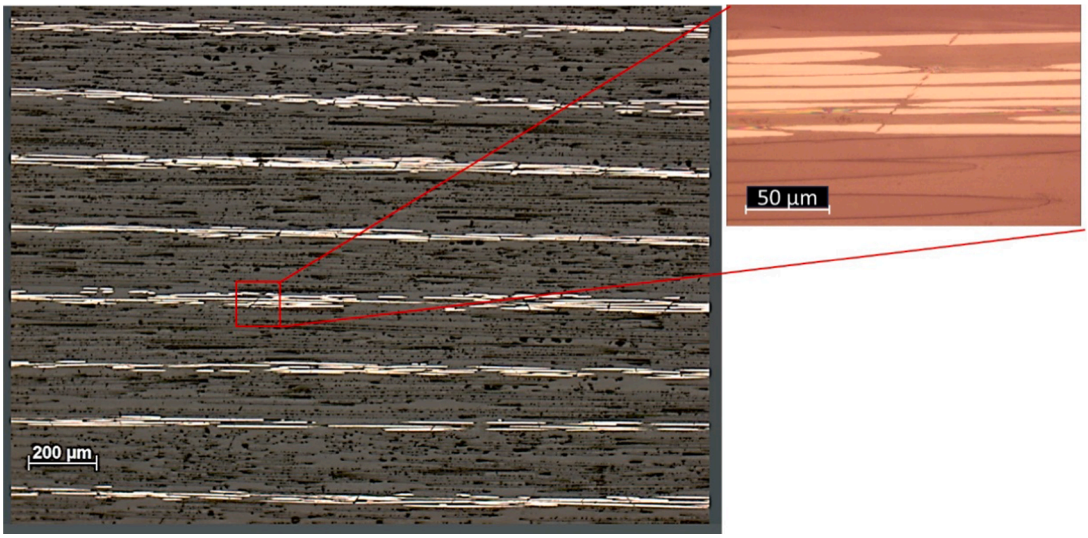

Fig. B1. Damage pattern of $[SG_1/(M55_1/SG_1)_{17}]$ at −0.80 % showing fragmentation of the carbon plies and the intact glass layers.

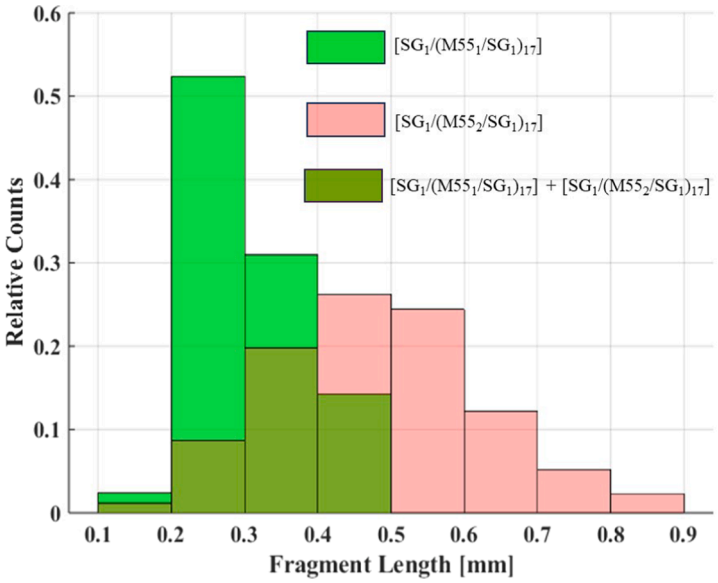

Fig. B2. Distribution of the fragment lengths after applying −0.80 % strain for $[SG_1/(M55_1/SG_1)_{17}]$ and $[SG_1/(M55_2/SG_1)_{17}]$ hybrids. Overlapping columns are described by the notation $[SG_1/(M55_1/SG_1)_{17}] + [SG_1/(M55_2/SG_1)_{17}]$.

Appendix C. Damage pattern of the asymmetric thin-ply hybrid composites under four-point bending

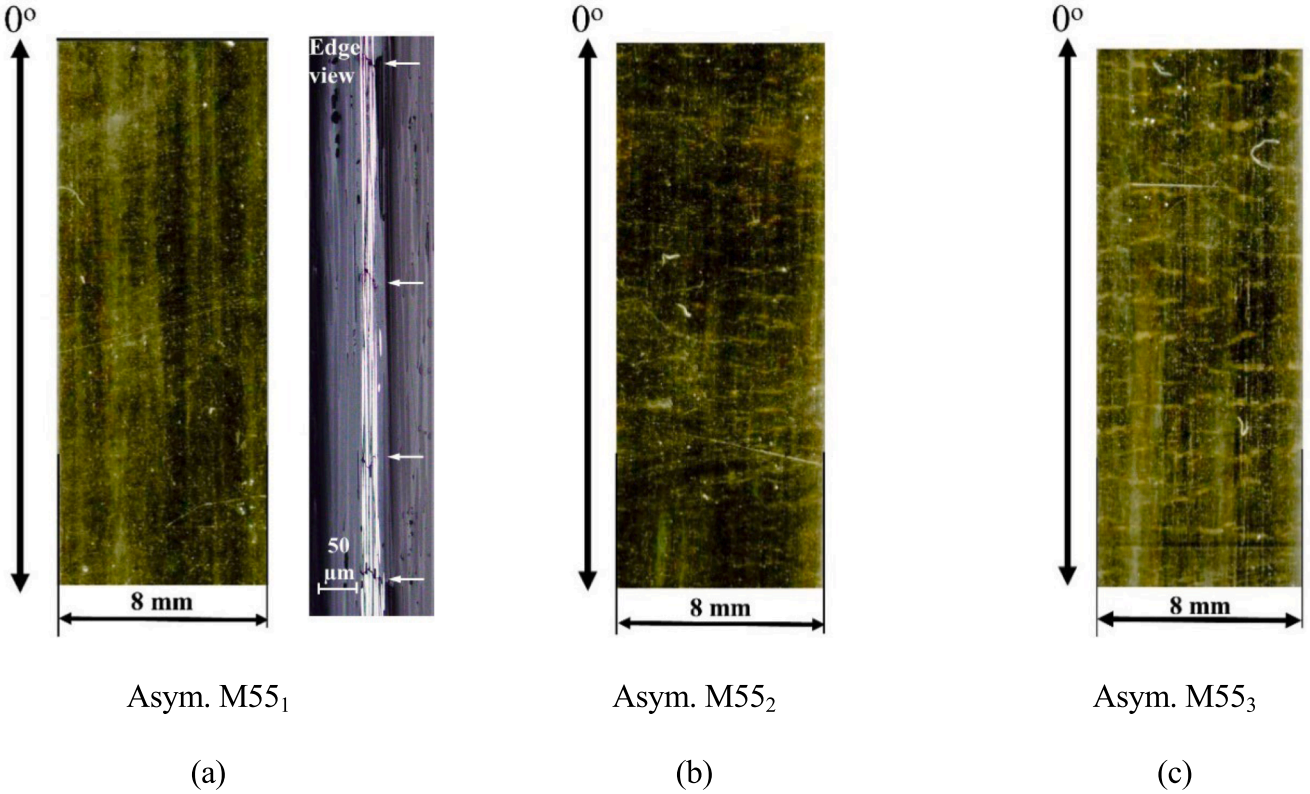

Fig. C1. Damage appearance on the surface and edge of different asymmetric hybrid laminates after four-point bending until −0.80 % strain, with the black arrows showing the 0^o fibre direction and white arrows showing fractures in the CF/EP layer under optical microscope.

Data availability

No data was used for the research described in the article.

References

[1] Wisnom MR, et al. High performance ductile and pseudo-ductile polymer matrix composites: a review. *Compos Part A Appl Sci Manuf*, 2023;181(June 2023):2024. https://doi.org/10.1016/j.compositesa:2024.108029.
[2] Czél G, Jalalvand M, Wisnom MR. Design and characterisation of advanced pseudo-ductile unidirectional thin-ply carbon/epoxy-glass/epoxy hybrid composites.

Compos Struct, 2016;143:362–70. https://doi.org/10.1016/j.compstruct.2016.02.010.
[3] Sihn S, Kim RY, Kawabe K, Tsai SW. Experimental studies of thin-ply laminated composites. *Compos Sci Technol*, 2007;67:996–1008. https://doi.org/10.1016/j.compscitech.2006.06.008.
[4] Yokozeki T, Kuroda A, Yoshimura A, Ogasawara T, Aoki T. Damage characterization in thin-ply composite laminates under out-of-plane transverse loadings. *Compos Struct*, 2010;93(1):49–57. https://doi.org/10.1016/j.compstruct.2010.06.016.
[5] Saito H, et al. Effect of ply-thickness on impact damage morphology in CFRP laminates. *J Reinf Plast Compos*, 2011;30(13):1097–106. https://doi.org/10.1177/0731684411416532.
[6] Arteiro A, Catalanotti G, Xavier J, Camanho PP. Notched response of non-crimp fabric thin-ply laminates. *Compos Sci Technol*, 2013;79:97–114. https://doi.org/10.1016/j.compscitech.2013.02.001.
[7] Amacher R, Cugnoni J, Botsis J, Sorensen L, Smith W, Dransfeld C. Thin ply composites: experimental characterization and modeling of size-effects. *Compos Sci Technol*, 2014;101:121–32. https://doi.org/10.1016/j.compscitech.2014.06.027.
[8] Arteiro A, Catalanotti G, Xavier J, Linde P, Camanho PP. Effect of tow thickness on the structural response of aerospace-grade spread-tow fabrics. Compos Struct 2017;179:208–23. https://doi.org/10.1016/j.compstruct.2017.06.047.
[9] Czél G, Wisnom MR. Demonstration of pseudo-ductility in high performance glass/epoxy composites by hybridisation with thin-ply carbon prepreg. *Compos Part A Appl Sci Manuf*, 2013;52:23–30. https://doi.org/10.1016/j.compositesa:2013.04.006.
[10] Jalalvand M, Czél G, Wisnom MR. Numerical modelling of the damage modes in UD thin carbon/glass hybrid laminates. *Compos Sci Technol*, 2014;94:39–47. https://doi.org/10.1016/j.compscitech.2014.01.013.
[11] Jalalvand M, Czél G, Wisnom MR. Damage analysis of pseudo-ductile thin-ply UD hybrid composites – A new analytical method. *Compos Part A Appl Sci Manuf*, Feb. 2015;69:83–93. https://doi.org/10.1016/j.compositesa:2014.11.006.
[12] Jelf PM, Fleck NA. Compression failure mechanisms in unidirectional composites. *J Compos Mater*, 1992;26(18):2706–26. https://doi.org/10.1177/002199839202601804.
[13] Budiansky B, Fleck Na. Compressive failure of fibre composites. *J Mech Phys Solids* 1993;41(1):183–211. https://doi.org/10.1016/0022-5096(93)90068-Q.
[14] Berbinau P, Soutis C, Guz IA. Compressive failure of 0° unidirectional carbon-fibre-reinforced plastic (CFRP) laminates by fibre microbuckling. *Compos Sci Technol*, 1999;59(9):1451–5. https://doi.org/10.1016/S0266-3538(98)00181-X.
[15] Wisnom MR, Atkinson JW. Compressive failure due to shear instability: Experimental investigation of waviness and correlation with analysis. *J Reinf Plast Compos*, 1996;15(4):420–39. https://doi.org/10.1177/073168449601500404.
[16] Wisnom MR. The effect of fibre misalignment on the compressive strength of unidirectional carbon fibre/epoxy. *Composites* 1990;21(5):403–7.
[17] Daniel IM, Hsiao HM. Is there a thickness effect on compressive strength of unnotched composite laminates? *Int J Fract*, 1999;95(1–4):143–58. https://doi.org/10.1023/A:1018692032303.
[18] Hancox NL. The compression strength of unidirectional carbon fibre reinforced plastic. *J Mater Sci*, 1975;10(2):234–42. https://doi.org/10.1007/BF00540347.
[19] Yokozeki T, Aoki Y, Ogasawara T. Experimental characterization of strength and damage resistance properties of thin-ply carbon fiber/toughened epoxy laminates. *Compos Struct*, 2008;82(3):382–9. https://doi.org/10.1016/j.compstruct.2007.01.015.
[20] Yan B, Zhu S, Tong M, Pan S. Experimental study on the mechanical properties of laminates made of thin carbon fiber plies. *Compos Struct*, 2020;245(October 2019):112336. https://doi.org/10.1016/j.compstruct.2020.112336.
[21] Montagnier O, Hochard C. Compression characterization of high-modulus carbon fibers. *J Compos Mater*, 2005;39(1):35–49. https://doi.org/10.1177/0021998305046433.
[22] Czél G, Jalalvand M, Wisnom MR. Hybrid specimens eliminating stress concentrations in tensile and compressive testing of unidirectional composites. *Compos Part A Appl Sci Manuf*, 2016;91:436–47. https://doi.org/10.1016/j.compositesa:2016.07.021.
[23] J. G. Haberle and F. L. Matthews, "An improved technique for compression testing of unidirectional fibre-reinforced plastics ; development and results," vol. 25, no. 5, pp. 358–371, 1994.
[24] Wisnom MR, Atkinson JW, Jones MI. Reduction in compressive strain to failure with increasing specimen size in pin-ended buckling tests. *Compos Sci Technol*, 1997;57(9–10):1303–8. https://doi.org/10.1016/S0266-3538(97)00057-2.
[25] Suwarta P, Czel G, Fotouhi M, Rycerz J, Wisnom M. Pseudo-ductility of Unidirectional Thin Ply hybrid composites in longitudinal compression. In: in *ASC 33rd Annual Technical Conference*; 2018. https://doi.org/10.12783/asc33/25987.
[26] Torayca, "M55J Data Sheet," Toray. Accessed: Jun. 03, 2022. [Online]. Available: https://www.toraycma.com/wp-content/uploads/M55J-Technical-Data-Sheet-1.pdf.
[27] Czél G, Jalalvand M, Wisnom MR. Demonstration of pseudo-ductility in unidirectional hybrid composites made of discontinuous carbon/epoxy and continuous glass/epoxy plies. *Compos Part A Appl Sci Manuf*, 2015;72:75–84. https://doi.org/10.1016/j.compositesa:2015.01.019.
[28] Wu X, Fuller JD, Wisnom MR. Role of fibre fragmentation on pseudo-ductility of thin-ply [±277/0]s carbon fibre laminates with high modulus 0° plies under compressive and flexural loading. *Compos Sci Technol* 2020;199(April):108377. https://doi.org/10.1016/j.compscitech.2020.108377.
[29] Hallett SR, Wisnom MR. Numerical investigation of progressive damage and the effect of layup in notched tensile tests. *J Compos Mater*, 2006;40(14):1229–45. https://doi.org/10.1177/0021998305057432.
[30] Xie M, Adams DF. Effect of specimen tab configuration on compression testing of composite materials. *J Compos Mater*, 1995;29(12):1581–600. https://doi.org/10.1177/002199839502901203.
[31] V. Keryvin, A. Marchandise, and J. C. Grandidier, "Non-linear elastic longitudinal behaviour of continuous carbon fibres/epoxy matrix composite laminae: Material or geometrical feature?," *Compos. Part B Eng.*, vol. 247, no. March, p. 110329, 2022, doi: 10.1016/j.compositesb.2022.110329.
[32] Dobb MG, Johnson DJ, Park CR. Compressional behaviour of carbon fibres. *J Mater Sci*, 1990;vol. 25(2 A):829–34. https://doi.org/10.1007/BF03372169.
[33] Kelly A, Tyson WR. Tensile properties of fibre reinforced metals: copper-tungsten and copper-molybdenum. *J Mech Phys Solids* 1965;13:329–50. https://doi.org/10.1016/0022-5096(65)90035-9.
[34] Cui WC, Wisnom MR, Jones M. Failure mechanisms in three and four point short beam bending tests of unidirectional glass/epoxy. *J Strain Anal Eng Des*, 1992;27(4):235–43. https://doi.org/10.1243/03093247V274235.
[35] Murphey TW, Peterson ME, Grigoriev MM, Babuska V. Large strain four-point bending of thin unidirectional composites. *J Spacecr Rockets* 2015;52(3):882–95. https://doi.org/10.2514/1.A32841.
[36] Petrossian Z, Wisnom MR. Parametric study of delamination in composites with discontinuous plies using an analytical solution based on fracture mechanics. *Compos Part A Appl Sci Manuf*, 1998;29(4):403–14. https://doi.org/10.1016/S1359-835X(97)00102-4.